

Axial instability of a free-surface front in a partially filled horizontal rotating cylinder

A. E. Hosoi

Department of Mathematics, Massachusetts Institute of Technology, Cambridge, Massachusetts 02139

L. Mahadevan

*Division of Mechanics and Materials, Mechanical Engineering 1-310,
Massachusetts Institute of Technology, Cambridge, Massachusetts 02139*

(Received 26 November 1997; accepted 23 September 1998)

We investigate the axial instability of the free-surface front of a viscous fluid in a horizontal cylinder rotating about its longitudinal axis. A simplified model equation for the evolution of the free surface is derived and includes the effects of gravity, capillarity, inertia, and viscosity. This equation is solved numerically to determine the base state with no axial variation, and a numerical linear stability analysis is carried out to examine the onset of unstable axial modes. Various computational results are presented for the wavelength of the axial instability. Inertia is found to play an important role in the onset of the instability and the wavelength of the instability λ satisfies the power law $\lambda \sim \gamma^{1/3}$, where γ is surface tension. Finally some numerical simulations of the simplified evolution equation are presented to show that they can capture the steady shark-teeth patterns observed in recent experiments [R. E. Johnson, in *Engineering Science, Fluid Dynamics: A Symposium to Honor T. Y. Wu* (World Scientific, Singapore, 1990), pp. 435–449; S. T. Thoroddsen and L. Mahadevan, “Experimental studies of the instabilities in a partially filled horizontal rotating cylinder,” *Exp. Fluids* **23**, 1 (1997)]. © 1999 American Institute of Physics. [S1070-6631(99)01001-6]

I. INTRODUCTION

Coating flows are fluid flows which lead to thin films of liquid forming onto surfaces as a result of external forces associated with inertia, viscosity, gravity, surface tension, etc. Besides being important in a number of industrial processes,¹ they form an interesting system in which to study free-surface instabilities in hydrodynamics.

In this paper, we consider the axial instability of the free surface of a viscous fluid partially filling a horizontally rotating cylinder, shown in Fig. 1. At zero angular velocity, the fluid is stationary and lies in a pool at the bottom of the cylinder, while at very high angular velocity, the fluid rotates rigidly with the cylinder and forms a homogeneous film that coats the cylinder uniformly. Much of the early work on coating flows in this geometry focused on this latter limiting case of nearly rigid rotation;^{2,3} these and other studies are reviewed by Ruschak in Ref. 4. For moderate rotation rates when gravitational effects are no longer perturbative, many interesting instabilities and patterns have been seen.^{5–9} Some of these patterns resemble those found in the flow down an inclined plane;^{10,11} others resemble those found in flows between two horizontal cylinders in the so-called printer's instability problem.¹² However the case considered here has the unique advantage that the flow is confined. This means that the cylindrical surface is continuously wetted so that any concerns involving the complicated physics associated with the dynamics of contact lines and precursor films are eliminated. The price for this convenience is that the mathematical analysis is complicated by the presence of a curved substrate which introduces an additional length scale.

Much of the previous work on this system was stimulated by a paper by Moffatt¹³ who used a kinematic wave theory to study the behavior of a viscous film coating the exterior of a cylinder, and presented some qualitative experiments. More recently, Johnson⁵ derived a lubrication approximation, with the dominant balance between gravity and viscosity, and showed that the equations are always axially stable for intermediate wave lengths. In recent work,^{7,8} the focus has been on two-dimensional steady interior coating flows that account for the effects of surface tension.

Here, we build on these results by uncovering some unsteady two-dimensional flows, analyze the axial stability of the steady two-dimensional flows, and simulate some three-dimensional solutions using a simplified model equation that describes these free-surface flows. In Sec. II we formulate the problem and make the equations dimensionless. We then derive an asymptotic equation for the height of the free surface. This requires the use of a modified lubrication theory very similar to that in Refs. 14 and 8, but accounts for inertia perturbatively. In Sec. III, we present computational results for two-dimensional steady and unsteady coating flows. In Sec. IV we analyze the axial stability of the steady coating flow and present a scaling law for the dominant wavelength of the axial instability. Three-dimensional flows are presented in Sec. V showing the shark-teeth patterns observed in recent experiments.^{5,6} We close with a discussion of our results in Sec. VI.

II. AN APPROXIMATE MODEL

The geometry and notation used in the problem are shown in Fig. 1. Since the analysis of the three-dimensional

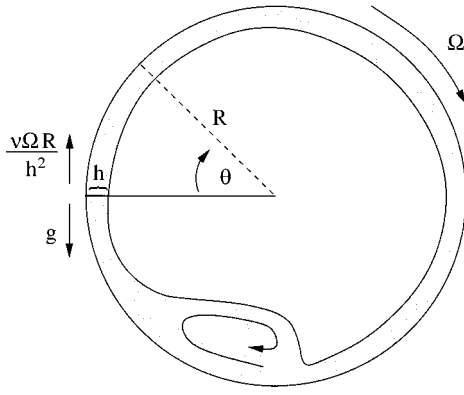


FIG. 1. Schematic diagram of a cross section of the cylinder. The dominant forces for a thin film are shown on the left. The arrow at the bottom indicates the recirculation region.

Navier–Stokes equations in the presence of a free surface is complicated, our first goal is to find an effective evolution equation for the free surface, $h(\theta, z, t)$, in a manner similar to classical lubrication theory.¹⁵ We assume that the fluid has viscosity μ , density ρ , kinematic viscosity $\nu = \mu/\rho$, and surface tension γ , and sits in a cylinder of radius R that rotates at an angular velocity Ω . Since the fluid is assumed to be incompressible, the continuity equation and the Navier–Stokes equations of motion are given by¹⁶

$$\nabla \cdot \mathbf{u} = 0, \quad (2.1)$$

$$\rho(\mathbf{u}_t + (\mathbf{u} \cdot \nabla)\mathbf{u}) = -\nabla p + \nu \nabla^2 \mathbf{u} + \mathbf{g}. \quad (2.2)$$

The geometry naturally leads us to cylindrical polar coordinates r, θ, z with unit radial, azimuthal and axial vectors $\hat{\mathbf{r}}, \hat{\boldsymbol{\theta}}, \hat{\mathbf{z}}$, respectively. Then the fluid velocity $\mathbf{u}(r, \theta, z) = u\hat{\mathbf{r}} + v\hat{\boldsymbol{\theta}} + w\hat{\mathbf{z}}$, $p(r, \theta, z)$ is the pressure, and gravity $\mathbf{g} = -g \sin \theta \hat{\mathbf{r}} - g \cos \theta \hat{\boldsymbol{\theta}}$. On writing Eqs. (2.1)–(2.2) in cylindrical coordinates we get¹⁶

$$\frac{(ru)_r}{r} + \frac{v_\theta}{r} + w_z = 0, \quad (2.3)$$

$$\begin{aligned} \frac{Du}{Dt} - \frac{v^2}{r} &= -\frac{p_r}{\rho} + \nu \left(\Delta u - \frac{u}{r^2} - \frac{2v_\theta}{r^2} \right) - g \sin \theta, \\ \frac{Dv}{Dt} + \frac{uv}{r} &= -\frac{p_\theta}{\rho r} + \nu \left(\Delta v + \frac{2u_\theta}{r^2} - \frac{v}{r^2} \right) - g \cos \theta, \end{aligned} \quad (2.4)$$

$$\frac{Dw}{Dt} = -\frac{p_z}{\rho} + \nu \Delta w,$$

where

$$\frac{D}{Dt} \equiv \partial_t + u \partial_r + \frac{v}{r} \partial_\theta + w \partial_z,$$

$$\Delta \equiv \frac{\partial_r(r \partial_r)}{r} + \frac{\partial_\theta^2}{r^2} + \partial_z^2,$$

and subscripts denote partial derivatives. The boundary conditions on the cylindrical surface $r=R$ are given by

$$u=0, \quad v=\Omega R, \quad w=0. \quad (2.5)$$

On the free surface, $r=R-h(z, \theta, t)$, the boundary conditions are

$$\mathbf{n} \cdot \boldsymbol{\sigma} \cdot \mathbf{n} = \gamma \kappa, \quad \mathbf{t}_i \cdot \boldsymbol{\sigma} \cdot \mathbf{n} = 0, \quad i=1,2, \quad (2.6)$$

i.e., the normal stresses are balanced by surface tension and there are no tangential stresses at the free surface. Here $\boldsymbol{\sigma}$ is the stress tensor, \mathbf{t}_i ; $i=1,2$ are the tangents to the surface and $\mathbf{n}=\mathbf{t}_1 \times \mathbf{t}_2$ is the outward normal to the free surface; γ is surface tension and κ is the curvature. The components of the stress tensor $\boldsymbol{\sigma}$ are given by

$$\begin{aligned} \sigma^{rr} &= -p + 2\mu u_r, \quad \sigma^{r\theta} = \mu \left(v_r + \frac{u_\theta}{r} - \frac{v}{r} \right), \\ \sigma^{rz} &= \mu(w_r + u_z), \\ \sigma^{\theta\theta} &= -p + 2\mu \left(\frac{u}{r} + \frac{v_\theta}{r} \right), \quad \sigma^{\theta z} = \mu \left(v_z + \frac{w_\theta}{r} \right), \\ \sigma^{zz} &= -p + 2\mu w_z. \end{aligned} \quad (2.7)$$

The tangents and the normal to the free-surface are given by

$$\hat{\mathbf{t}}_1 = \frac{-h_\theta \hat{\mathbf{r}} + (R-h) \hat{\boldsymbol{\theta}}}{\sqrt{h_\theta^2 + (R-h)^2}}, \quad \hat{\mathbf{t}}_2 = \frac{-h_z \hat{\mathbf{r}} + \hat{\mathbf{z}}}{\sqrt{h_z^2 + 1}}, \quad \hat{\mathbf{n}} = \frac{\hat{\mathbf{t}}_1 \times \hat{\mathbf{t}}_2}{|\hat{\mathbf{t}}_1 \times \hat{\mathbf{t}}_2|}, \quad (2.8)$$

with $\hat{\mathbf{t}}_1 \times \hat{\mathbf{t}}_2 \propto (R-h) \hat{\mathbf{r}} + h_\theta \hat{\boldsymbol{\theta}} + (R-h) h_z \hat{\mathbf{z}}$. The kinematic boundary condition on the free surface is given by

$$\frac{D(r-R+h)}{Dt} = 0. \quad (2.9)$$

We now consider the appropriate length and time scales with which to make the equations dimensionless. Balancing the viscous forces against the force of gravity gives a characteristic length scale for the thin film $L = (\nu \Omega R / g)^{1/2}$.^{14,8} There are two characteristic time scales given by $T = R^2 / \nu$ which is a viscous time scale and $T' = 1/\Omega \ll T$ which is a time scale associated with rotation. Since events equilibrate themselves quickly over the fast time scale, we rescale the variables using the slow time scale T and the length L and define three dimensionless parameters

$$\beta \equiv \alpha \text{Re} = \sqrt{\frac{(\Omega R)^3}{g \nu}} \sim O(1),$$

$$\alpha \equiv \frac{L}{R} = \sqrt{\frac{\nu \Omega}{R g}} \ll 1,$$

$$B^{-1} = \frac{\gamma}{\rho g R^2} \ll 1,$$

where $\text{Re} = R^2 \Omega / \nu$ is the Reynolds number, and characterizes the ratio of inertial to viscous forces; B^{-1} is the inverse of the Bond number, and characterizes the ratio of capillary and gravitational forces; and α is the ratio of viscous to gravitational forces. Note that β is a scaled Reynolds number. By defining $\beta \equiv \alpha \text{Re}$ we consider intermediate Reynolds number regimes corresponding to $\text{Re} \sim O(1/\alpha)$. This corresponds to the range of experimental interest, and in particular to the region in phase space,⁶ where the shark-teeth patterns exist.

Then the dimensionless variables in the problem become

$$\begin{aligned}\tilde{u} &= \frac{1}{\alpha} \frac{u}{\Omega R}, \quad \tilde{v} = \frac{v}{\Omega R}, \quad \tilde{w} = \frac{w}{\Omega R}, \\ \tilde{t} &= \frac{\nu}{R^2} t, \quad \tilde{r} = \frac{1}{\alpha} \left(1 - \frac{r}{R}\right), \quad \tilde{z} = \frac{z}{R}, \\ \tilde{p} &= \frac{p}{\rho g R}, \quad \eta = \frac{h}{\alpha R}.\end{aligned}\quad (2.10)$$

Here $\eta = \eta(\theta, z, t)$ is the rescaled height of the free surface and \tilde{r} is measured inwards from the wall of the cylinder; i.e., $\tilde{r} = 0$ when $r = R$. We have scaled the radial velocity u and the radial coordinate r by α as is usual in lubrication theory. However, here α is not simply the aspect ratio but instead measures the relative strength of viscous to gravitational forces. Rewriting Eqs. (2.1)–(2.2) in terms of the dimensionless variables defined in Eq. (2.10) and the parameters α , β , and B^{-1} yields, on dropping the 's,

$$-[(1 - \alpha r)u]_r + v_\theta + (1 - \alpha r)w_z = 0, \quad (2.11)$$

$$\begin{aligned}\alpha^2 \beta \frac{v^2}{(1 - \alpha r)} &= -p_r + \alpha^2 \nabla_{sc}^2 u - \alpha \sin \theta + O(\alpha^3), \\ \alpha^2 v_t + \alpha \beta (\mathbf{u} \cdot \nabla_{sc})v + \alpha^2 \beta \frac{vu}{(1 - \alpha r)} \\ &= -\frac{1}{(1 - \alpha r)} p_\theta + \nabla_{sc}^2 v - \frac{\alpha^2 v}{(1 - \alpha r)^2} \cos \theta + O(\alpha^3),\end{aligned}\quad (2.12)$$

$$\alpha^2 w_t + \alpha \beta (\mathbf{u} \cdot \nabla_{sc})w = -p_z + \nabla_{sc}^2 w.$$

Here

$$\begin{aligned}\mathbf{u} \cdot \nabla_{sc} &= -u \partial_r + \frac{v}{(1 - \alpha r)} \partial_\theta + w \partial_z, \\ \nabla_{sc}^2 &= \partial_r^2 - \frac{\alpha}{(1 - \alpha r)} \partial_r + \frac{\alpha^2}{(1 - \alpha r)^2} \partial_\theta^2 + \alpha^2 \partial_z^2.\end{aligned}$$

The boundary conditions (2.5) at the cylindrical surface $r = 0$ written in dimensionless form yield

$$u = w = 0, \quad v = 1 \quad (2.13)$$

at $r = 0$, while the boundary conditions (2.6) at the free surface $r = \eta$ written in dimensionless form yield

$$\begin{aligned}\alpha v_r + \alpha^2 (v - 2\eta v_r) + O(\alpha^3) &= 0, \\ \alpha w_r - \alpha^2 \eta w_r + O(\alpha^3) &= 0, \\ -p + 5\alpha^2 p \eta^2 - 2\alpha^2 (u_r + v_r \eta_\theta + w_r \eta_z) + O(\alpha^3) \\ &= -B^{-1} \kappa,\end{aligned}\quad (2.14)$$

where

$$\begin{aligned}\kappa &= 1 + \alpha (\eta + \eta_{zz} + \eta_{\theta\theta}) \\ &+ \alpha^2 (2\eta \eta_{\theta\theta} + \eta^2 + \tfrac{1}{2}(\eta_\theta^2 - \eta_z^2)) + O(\alpha^3).\end{aligned}$$

In order to get a low-dimensional description that is more easily amenable to numerical simulation, we make use of the presence of the small parameter α . Integrating the

continuity Eq. (2.11) over the depth of the film, and using the rescaled kinematic boundary condition from Eq. (2.9),

$$\frac{\alpha}{\beta} \eta_t + u + \frac{v}{(1 - \alpha \eta)} \eta_\theta + w \eta_z = 0$$

to eliminate the radial velocity u , we get

$$\frac{\alpha}{\beta} \eta_t + q_\theta + Q_z = 0, \quad (2.15)$$

where the fluxes q and Q are

$$q(\theta, z, t) = \int_0^\eta v dr, \quad Q(\theta, z, t) = \int_0^\eta (1 - \alpha r) w dr. \quad (2.16)$$

Equation (2.15) is valid only in the limit $\beta \geq O(1)$, which is consistent with our choice of the time scale $T = R^2/\nu$ to make our variables dimensionless in Eq. (2.12). When $\beta \rightarrow 0$ the relevant time scale is $T' = 1/\Omega$ and Eq. (2.15) becomes $(1 - \alpha \eta) \eta_t + q_\theta + Q_z = 0$, considered earlier in Ref. 8. To determine the dimensionless azimuthal and axial velocities in Eq. (2.16), we approximate the dimensionless velocity and pressure fields by expanding them in the small parameter α , and write

$$\mathbf{u} = \mathbf{u}_0(r, \theta, z, t) + \alpha \mathbf{u}_1(r, \theta, z, t) + \alpha^2 \mathbf{u}_2(r, \theta, z, t) + \dots, \quad (2.17)$$

$$p = p_0(r, \theta, z, t) + \alpha p_1(r, \theta, z, t) + \alpha^2 p_2(r, \theta, z, t) + \dots. \quad (2.18)$$

Next we substitute our expanded variables into Eqs. (2.12)–(2.14). Solving the resulting equations order by order yields the velocity and pressure fields in terms of η and its derivatives (see Appendix A). Keeping terms that are correct to $O(\alpha)$ for $v = v_0 + \alpha v_1$, $w = w_0 + \alpha w_1$, and $p = p_0 + \alpha p_1$ and substituting into Eq. (2.16) yields

$$\begin{aligned}q &= \eta - \tfrac{1}{3} \eta^3 \cos \theta + \alpha \{ \tfrac{1}{2} \eta^4 \cos \theta - \tfrac{1}{2} \eta^2 \\ &+ \tfrac{1}{3} \eta^3 (B^{-1} (\eta_\theta + \eta_{zz\theta} + \eta_{\theta\theta\theta}) + \eta_\theta \sin \theta) + \beta q_{I1} \},\end{aligned}\quad (2.19)$$

$$Q = \frac{\alpha}{3} \eta^3 \{ \eta_z \sin \theta + B^{-1} (\eta_z + \eta_{zzz} + \eta_{\theta\theta z}) \}, \quad (2.20)$$

where

$$\begin{aligned}q_{I1} &= -\frac{13}{420} \eta^7 \sin \theta \cos \theta \\ &+ (\frac{5}{24} \eta^4 - \frac{3}{40} \eta^6 \cos \theta) (\eta \cos \theta)_\theta + \frac{3}{40} \eta^5 \sin \theta.\end{aligned}$$

Equations (2.15), (2.19), and (2.20), subject to periodic boundary conditions in θ and no-slip conditions (in the θ direction) and no flux conditions (in the z direction) at the ends $z = \pm l$, where $2l$ is the length of the cylinder, define the complete system which we will solve numerically. The effects of inertia are weak, as we are assuming the dominant force balance is between viscosity and gravity, and appear in Eq. (2.19) as the terms premultiplied by β . However, we will later find a qualitative agreement with experiment even when β is relatively large. No additional equation is needed for the radial velocity u at this order since u_t appears only at $O(\alpha^4)$ in Eq. (2.12). This asymptotic reduction technique is similar

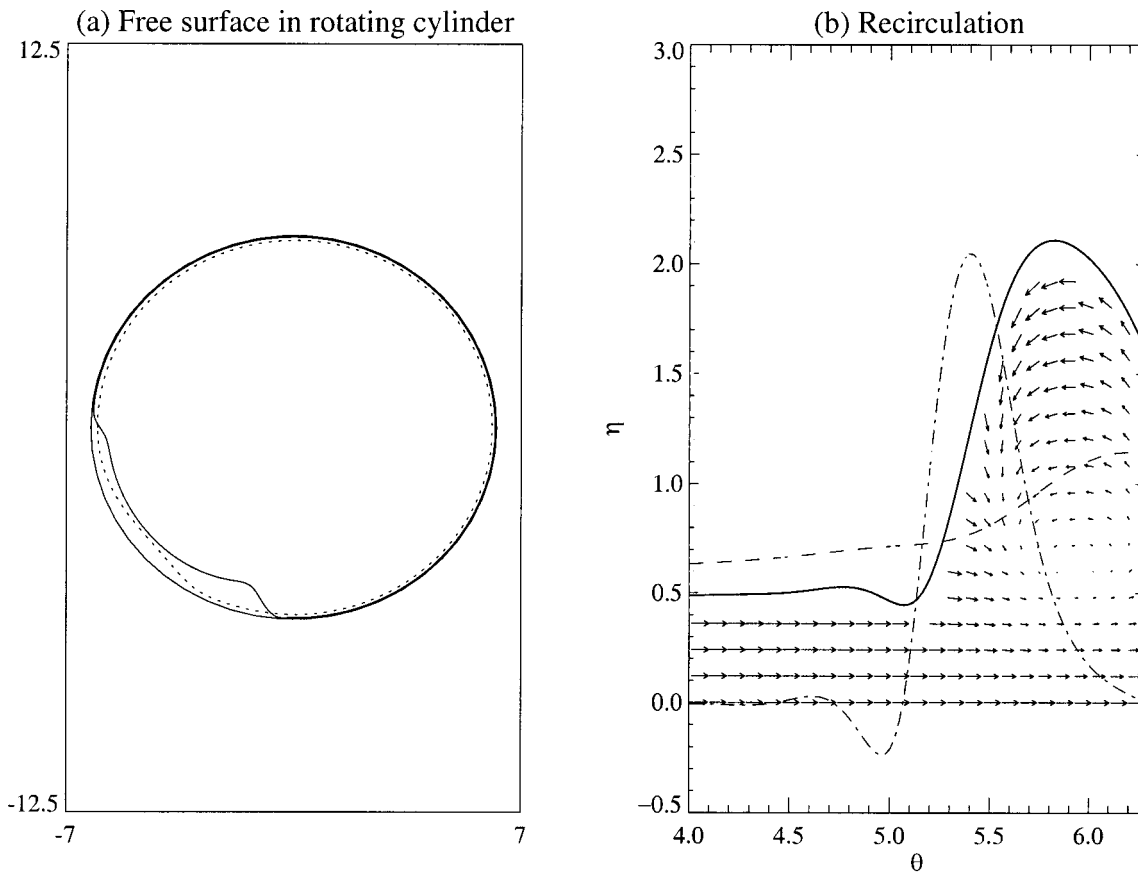


FIG. 2. Numerical solution of Eq. (2.11) with $Q=0$ showing the free-surface of the viscous fluid in a cylinder rotating clockwise. The parameter values used in (a) were $R=6.25$ cm, $\nu=49$ cm²/s, $\Omega=3.2$ Hz, $V=6.0\%$, and $B^{-1}=0.05$ which corresponds to $\alpha=0.04$ and $\beta=64.8$. The dotted line represents a solution with the same parameter values, but with $\beta=6.48$. (b) Here the solid line represents $R=6.25$ cm, $\alpha=0.04$, $\beta=25.92$, and $B^{-1}=0.5$; the dashed line corresponds to a reduced β of 6.48. The free surface has been “unwrapped” from the cylinder and plotted on a straight line; the bump corresponds to the puddle at the bottom of the cylinder. The arrows show the velocity field to leading order as given by Eq. (A3). We observe that for small β the ridge all but disappears. The dot-dashed line shows the shape of the most unstable eigenmode, h , which is localized near the leading edge of the front and is negligible elsewhere.

to the idea of center manifold reduction in dynamical systems¹⁷ and results in a significant simplification of the three-dimensional free-surface problems (2.1)–(2.9) when $\alpha \ll 1$. Once we have solved the scalar two-dimensional PDE (2.15) for $\eta(\theta, z, t)$ we can reconstruct the three-dimensional velocity field to $O(\alpha)$ by using the expressions $u=u_0 + \alpha u_1$, $v=v_0 + \alpha v_1$, $w=w_0 + \alpha w_1$ (see Appendix A).

III. TWO-DIMENSIONAL STEADY AND UNSTEADY FLOWS

We first consider two-dimensional flows with no axial variation so that $Q=0$. Since Eq. (2.15) is a nonlinear PDE we solve it numerically using a centered finite difference scheme and periodic boundary conditions, described in detail in Appendix B. Typical numerical results for steady flows are shown in Fig. 2. We observe that we can capture the recirculation region at the bottom of the cylinder with the cubic approximation to the azimuthal velocity profile and the regularization of the front due to surface tension inherent in the expansion to order $O(\alpha)$ in Eq. (2.19). Figure 2(a) shows that the surface is asymmetric with a ridge of fluid that has a steep front close to the bottom of the cylinder. The size of the ridge is proportional to the size of β which is a measure

of inertial effects. For example, the dotted lines in Fig. 2 show the profile for a lower value of β when the ridge has all but disappeared. We note that a similar ridge is found at the leading edge of a fluid flowing down an inclined plane¹⁰ where it triggers a transverse fingering instability. Inertia is unimportant in that case since gravitational forcing is constant. In the flow inside a cylinder this ridge all but disappears when inertia is small because the curvature of the substrate yields a differential gravitational forcing that is weakest in the vicinity of the ridge, at the bottom of the cylinder. However as inertial effects become larger they restore the imbalance between the rising and the falling film regions thus giving rise to a localized ridge. As we will shortly see the presence of this ridge is crucial in understanding of the transverse/axial instability of the steady two-dimensional flow.

As the problem parameters are varied, we also observe unsteady two-dimensional flows. When α , β are gradually increased, inertial forces begin to dominate over both gravitational and viscous forces. Then the localized ridge gets pulled over the top of the cylinder, while spreading out and reforms again at the bottom before the whole cycle repeats itself. This transition to a limit cycle from a stationary state

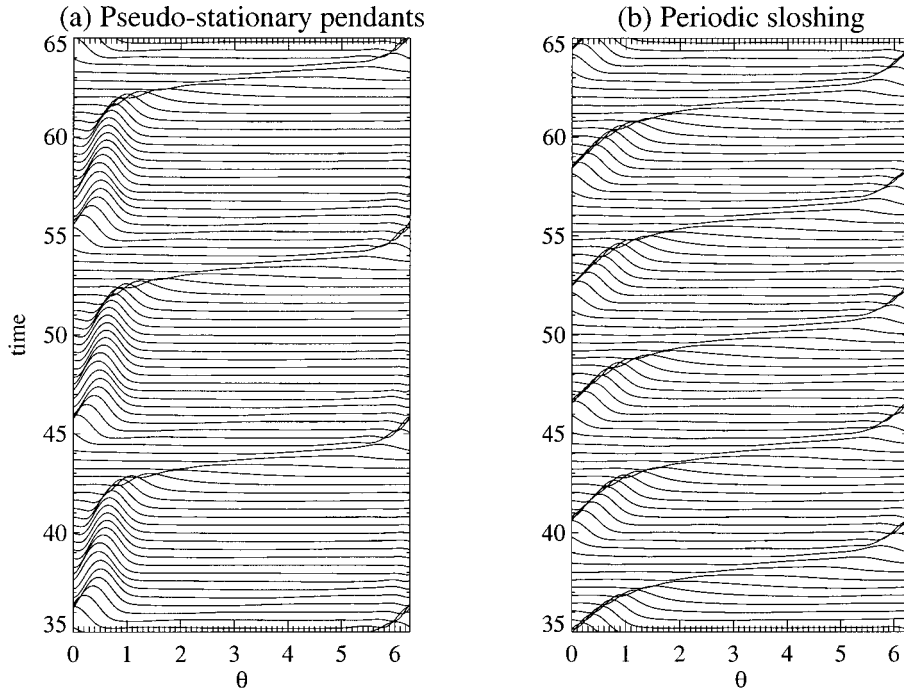


FIG. 3. Unsteady two-dimensional flows in a cylinder with 6% volume fraction of the fluid and $\alpha=0.055$, $B^{-1}=0.2$ shown in a space-time diagram. The solid lines show profiles of the free surface at a fixed time; time increases from one profile to the next moving vertically upwards. (a) When $\beta=24$, the spatially localized ridge remains stationary for long periods of time, but is periodically pulled over the top of the cylinder. (b) When $\beta=29$ the ridge exhibits limit cycle behavior.

is reminiscent of a saddle-node bifurcation in a finite-dimensional system,¹⁷ such as the damped-driven pendulum. The localized ridge is similar to the pendulum; as the forcing due to rotation becomes large enough, it is no longer capable of remaining stationary. Since it is a deformable object, it gets pulled over gradually, and reforms periodically. In Fig. 3(a), we show a space-time plot of the motion of a localized ridge for parameter values close to the bifurcation point when it is almost stationary for a long period of time before it gets pulled over. In Fig. 3(b), we show the limit cycle motion of the ridge that is periodically pulled over the top of the cylinder. These sloshing modes have been observed in three-dimensional flows experimentally⁶ where they take the form of pendants.

IV. AXIAL INSTABILITY OF STEADY TWO-DIMENSIONAL FLOWS

A. Linear stability analysis

To determine the wavelength of the shark-tooth instability, we axially perturb the two-dimensional steady state profile $\eta_0(\theta)$ computed in the previous section and calculate the linearly unstable axial modes. Substituting a perturbed profile of the form $\eta(\theta, z, t) = \eta_0(\theta) + \sum_{n=0}^N \epsilon h_n(\theta, t) \cos kz$, $k = \pi n/2l$, into Eqs. (2.15), (2.19), and (2.20) and keeping terms to order ϵ we obtain the set of linearized equations,

$$h_t + \frac{\beta}{\alpha} q_\theta - k^2 \frac{\beta}{3} \eta_0^3 (B^{-1} h_{\theta\theta} + g(\theta, k) h) = 0. \quad (4.1)$$

Here,

$$q = hf(\theta) + \frac{\alpha}{3} \eta_0^3 (B^{-1} h_{\theta\theta} + g(\theta, k) h_\theta) + \alpha \beta \left(\frac{5}{24} \eta_0^4 - \frac{3}{40} \eta_0^6 \cos \theta \right) (h \cos \theta)_\theta,$$

and

$$\begin{aligned} f(\theta) &\equiv 1 - \eta_0^2 \cos \theta + \alpha \{ 2 \eta_0^3 \cos \theta \\ &\quad + \eta_0^2 (B^{-1} (\eta_{0\theta\theta} + \eta_{0\theta\theta\theta}) + \eta_{0\theta} \sin \theta) \\ &\quad - \eta_0 + \beta f_I(\theta) \}, \\ f_I(\theta) &\equiv \frac{-13}{60} \eta_0^6 \sin \theta \cos \theta + \left(\frac{5}{8} \eta_0^3 - \frac{9}{20} \eta_0^5 \cos \theta \right) \\ &\quad \times (\eta_0 \cos \theta)_\theta + \frac{3}{8} \eta_0^4 \sin \theta, \\ g(\theta, k) &\equiv B^{-1} (1 - k^2) + \sin \theta. \end{aligned}$$

For each wave number k , this is of the form $h_t + \mathcal{L}h = 0$ so that the spectrum of the linear operator \mathcal{L} determines the stability of the system; eigenvalues that have negative real part indicate that the associated modal perturbations grow exponentially. In Fig. 4(a) we plot the eigenvalue with largest positive part $s(k)$ as a function of k , for $\alpha=0.04$ corresponding to the experimental parameters in Ref. 6, and two values of β . In both these cases we take $B^{-1}=0.5$; this is larger than the experimental values and is chosen to stabilize the numerical calculations. We see the existence of linearly unstable modes only when β is sufficiently large. This is consistent with Refs. 5 and 8, where it is shown that in the absence of inertia ($\beta=0$), the leading order system is always linearly stable to axial variations.

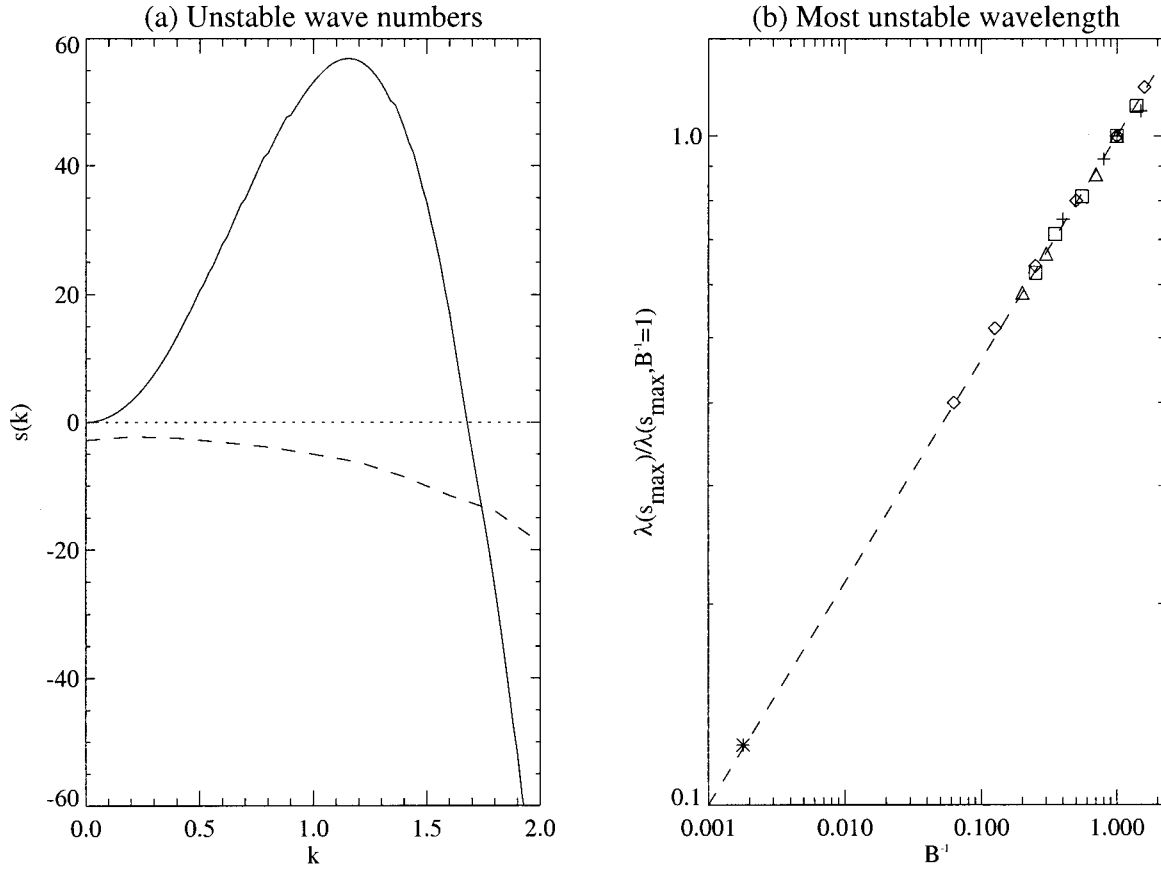


FIG. 4. Linear stability results for the rotating cylinder. (a) Here, $R=6.25$ cm, $\alpha=0.04$, $B^{-1}=0.5$, and $V=6\%$. The two curves in (a) show linear stability results for two values of β . The solid line corresponds to $\beta=25.92$ and the dashed line corresponds to $\beta=6.48$. As β gets smaller, the linear instability disappears. (b) Shows power law behavior for the wavelength of the teeth, $\lambda \sim \gamma^{1/3}$. Each symbol stands for a different set of parameters in our numerical simulations and the dotted line marks the curve $(B^{-1})^{1/3}$. Here B^{-1} is the rescaled surface tension. \diamond , $R=6.25$ cm, $\nu=49$ cm²/s, $\Omega=3.2$ Hz, and $V=6.0\%$. Δ , $R=6.25$ cm, $\nu=48$ cm²/s, $\Omega=2.7$ Hz, and $V=5.5\%$. $+$, $R=8.0$ cm, $\nu=55$ cm²/s, $\Omega=2.4$ Hz, and $V=6.0\%$. \square , $R=4.5$ cm, $\nu=30$ cm²/s, $\Omega=3.6$ Hz, and $V=6.0\%$. $*$ is an experimental point taken from Ref. 6 with the same parameters as the \diamond 's. Unfortunately we are unaware of experiments that vary surface tension, hence we show only one experimental point here corresponding to the surface tension on a water/air interface, $\gamma \sim 69$ dyn/cm.

Additionally we find that the wavelength of the teeth from our three-dimensional numerical simulations (see Sec. V) matches the wavelength of the teeth predicted by this linear stability analysis within expected error. This error occurs due to the finite length of the cylinder used in our simulations as compared to the infinite cylinder assumed in the stability calculations.

B. Mechanisms of the instability

The physical cause of the instability can be understood by looking at Fig. 2. Due to inertial effects, a localized ridge forms near the bottom of the cylinder. This ridge is axially unstable to both a Rayleigh-type capillary instability^{18,19} and an instability driven by the body forces on the fluid. To determine which is dominant, we perform an energy analysis similar to that in Spaid and Homsy.²⁰

First, we define a mechanical energy associated with the perturbation,

$$E = \frac{1}{2} \int_0^{2\pi} h^2 d\theta = \frac{1}{2} \langle h^2 \rangle. \quad (4.2)$$

Then by taking an inner product of Eq. (4.1) with h , we can determine whether a small perturbation, h , acts to increase or decrease the energy in the system. Terms that remove energy are stabilizing, whereas terms that add energy are destabilizing. To the lowest order, $\langle \alpha h_t / \beta + \mathcal{L}h, h \rangle = 0$ gives

$$\frac{\alpha}{\beta} E_t = \frac{\alpha}{2\beta} \langle h^2 \rangle_t = - \int_0^{2\pi} [(h - h\eta_0^2 \cos \theta)_\theta h] d\theta. \quad (4.3)$$

Here the dominant contribution to the integral comes from a localized region, as the perturbation, h , is concentrated in the vicinity of the front (see Fig. 2 (b)). The right-hand side represents the flow due to the body forces on the fluid. After a little manipulation (4.3) becomes

$$\frac{\alpha}{\beta} E_t + \int_0^{2\pi} \left[\left(\frac{1}{2} h^2 - h^2 \eta_0^2 \cos \theta \right)_\theta + h h_\theta \eta_0^2 \cos \theta \right] d\theta = 0.$$

The first term in the integral vanishes due to periodic boundary conditions, so the sign of the second term will determine stability to lowest order. By evaluating this term numerically, we find for all values of k ,

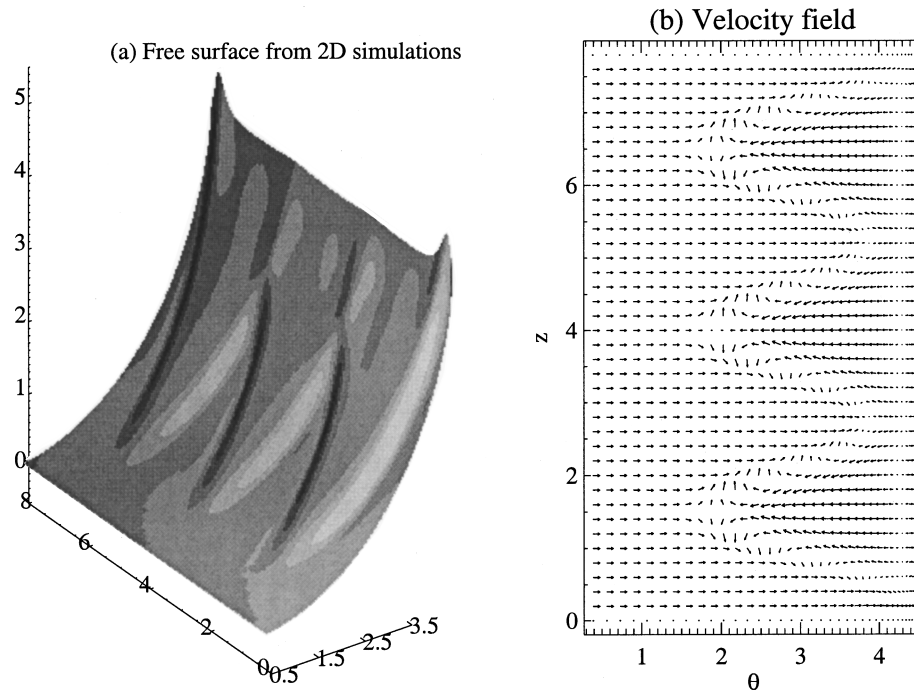


FIG. 5. Two-dimensional numerical results. This simulation was run with $R=4.5$ cm, $\nu=55$ cm²/s, $\Omega=2.0$ Hz, $V=5.0\%$, and $B^{-1}=0.01$ ($\alpha=0.04$, $\beta=18.3$). (a) Shows the free surface between $\theta=4.8$ and $\theta=2\pi$. (b) Shows the v and w velocities at the free surface. Note that each “tooth” is composed of two counter-rotating vortices.

$$\int_0^{2\pi} h h_{\theta} \eta_0^2 \cos \theta d\theta < 0.$$

Thus this contributes to an *increase* in energy and the term is destabilizing.

Since surface tension only comes in at $O(\alpha)$, we can conclude that the dominant destabilizing mechanism is due to gravitational and viscous forces. This is easily understood physically as the thick regions will tend to flow down the cylinder wall faster because thin regions will feel more viscous drag from the walls of the cylinder. This is completely analogous to the instability of a thin film flowing down an inclined plane scenario described by Spaid and Homsy.²⁰

However, this mechanism does not offer a way of selecting a wavelength. To determine the most unstable wavelength, we turn to capillary forces. A consequence of the classical capillary instability analysis is that the most unstable wavelength scales linearly with r_0 , the radius of a jet of fluid. By analogy, we expect the wavelength of our axial instability to scale linearly with W , the width of the ridge; this wavelength is determined numerically using the results of the linear stability analysis.

In the neighborhood of the ridge the two dominant forces are surface tension and viscosity. This is not contrary to our initial assumption that gravity and viscosity are the dominant forces in most of the fluid; it is only in a localized region around the ridge that surface tension becomes important due to the large curvature of the free surface. Following Ref. 11, we can define a characteristic width by balancing these two forces. In regions of high curvature (i.e., near the bump), $p \sim \gamma \kappa \sim \gamma H_{\theta\theta}$, where H is the height of the fluid. Then $-\nabla p / \rho \sim \nu \nabla^2 \mathbf{u}$ becomes

$$\frac{\gamma H}{\rho W^3} \sim \frac{\nu U}{H^2} \Rightarrow W \sim H \left(\frac{\gamma}{\rho \nu U} \right)^{1/3} = H \text{ Ca}^{-1/3},$$

where $\text{Ca} = \rho \nu U / \gamma$ is the capillary number and U is a characteristic velocity. Thus, we expect the wavelength of the teeth, λ , to scale like $\lambda \sim W \sim \gamma^{1/3}$. This is confirmed in Fig. 4(b). The only experimental data point available⁶ sits right on this line. It remains to be seen if further data confirm this scaling. This scaling of $\gamma^{1/3}$ can also be obtained from Eq. (2.19) by balancing η (the leading order viscous term) with $\alpha B^{-1} \eta^3 \eta_{\theta\theta} / 3$ (the leading order capillary term).

V. THREE-DIMENSIONAL STEADY FLOWS: SHARK-TEETH PATTERNS

In order to study the nonlinear behavior and saturation of the axial instability, we investigate the full set of Eqs. (2.15), (2.19), and (2.20), numerically in the unstable regime, using techniques described in Appendix B. Some numerical results for $\alpha=0.04$, $\beta=64.8$, $B^{-1}=0.05$ are shown in Fig. 5(a), and show a stationary pattern of shark-teeth. The individual teeth meet at cusp-like stagnation points, which are reminiscent of two-dimensional cusps in Stokes flows,²¹ while the rapid change in fluid depth that mark the teeth are like the “buckling” instabilities in circular hydraulic jumps in viscous flows.²²

Our simulations also show that the teeth develop first at the ends of the cylinder similar to what is observed experimentally.⁶ In the center of the cylinder, the fluid is driven only azimuthally, while at the ends, the fluid is also driven by the caps. This effectively results in a faster “pile-up” of fluid at the edges which allows the teeth to form more quickly there.

In Fig. 5(b), we show the azimuthal and axial velocity field corresponding to the free-surface shown in Fig. 5(a). The velocities are calculated using the asymptotic expressions given in Appendix A. We observe that there is an array of stagnation points associated with the shark-teeth. Their

number and arrangement agrees qualitatively with experiments.⁶ An analysis of the flow field in the neighborhood of these stagnation points would probably require a further simplification of the equations considered here; we leave this for the future.

It should be noted that the shark-teeth instability persists for parameter values $\alpha\beta > O(1)$ which is qualitatively in agreement with experiment. This is consistent with our scaling when one takes into account the localization of the front. In the bulk of the fluid, the flow is viscously dominated (as we assumed) and it is only in a small neighborhood of the front where there is an increased fluid depth that inertia becomes important. Similarly, surface tension is important only in the neighborhood of the front, where high curvature increases the relative importance of this effect. We should also add that in this region there is an additional length scale that we have not taken into account, dictated by the filling fraction of the fluid.

VI. DISCUSSION

We have considered the problem of free-surface instabilities in a partially-filled horizontal rotating cylinder. In order to simplify the analysis, we first derived an approximate evolution equation for the free-surface using the presence of a small parameter α that measures the ratio of the viscous to gravitational forces. This is preferred to the usual slenderness ratio used in lubrication theory, since here volume conservation in the confined geometry of a cylinder leads to large changes in the slenderness that cannot be accounted for in classical lubrication theory. This approach is similar to the Karman–Polhausen approach²³ in boundary layer theory, except that here the approximate velocity profile is derived using an asymptotic approximation and not presumed to be a high-order polynomial. In order to include the effects of capillary and inertial forces in our model, we used a higher order lubrication theory. This automatically introduces cubic and higher-order polynomial corrections to the azimuthal velocity profile that, unlike the simple quadratic profiles in lubrication theory, can account for regions of recirculation that exist in this problem. We numerically computed steady two-dimensional solutions of the approximate evolution equation without any axial variation. The effect of inertia was found to be significant in determining the shape of the coating film; for large values of the parameter β , a spatially localized ridge similar to those seen in inclined-plane flows appears. When perturbed axially, this ridge loses stability, mainly due to the fact that in the spanwise direction, fatter regions travel faster than thinner regions. The wavelength of the fastest growing mode was found to obey a simple scaling determined by the balance of capillary and viscous forces. We also computed some unsteady two-dimensional flows; these correspond to a periodic motion of the ridge as it gets pulled over the cylinder top. This transition to unsteady behavior comes into being via a saddle-node bifurcation as the forcing is increased beyond a critical threshold. In Fig. 6 we show the steady, and unsteady flow regimes as well as the regions of axial instability in a phase diagram in β – α space, for a filling fraction of 6% and B^{-1}

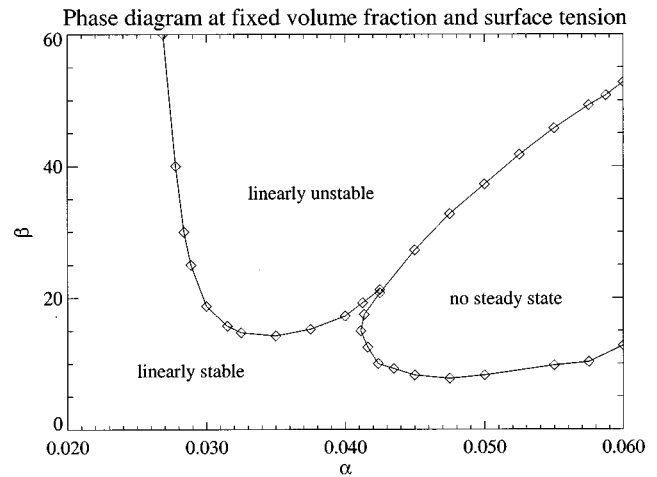


FIG. 6. Numerically calculated phase diagram at fixed volume fraction and surface tension showing the regions of linear stability and instability. Here “stable” means stable to wavelengths shorter than 1 m, and “no steady state” implies that no steady state was reached after 1000 cycles. We observe that for small β , when inertial effects are weak, the flow is linearly stable.

$=0.5$. The parameters α and β are chosen as they are the only two *independent* combinations of the physical parameters, Ω , ν , R , and g , that appear in the rescaled system.

Finally, we followed the nonlinear evolution of the axial instability and showed that this results in the stationary shark-teeth pattern observed in experiments. Of the many further questions that this study poses, perhaps the most interesting one involves a careful experimental and theoretical study of the three-dimensional flow in the neighborhood of these free-surface stagnation points. A combination of higher-order lubrication theories and a Karman–Polhausen boundary-layer approach may be useful in this venture.

ACKNOWLEDGMENTS

We gratefully thank S. Thoroddsen, J. Gollub, and D. P. Valette for their experimental data and all of the above plus T. F. Dupont, L. P. Kadanoff, M. P. Brenner, and G. M. Homsy for many useful discussions. This work made use of MRSEC Shared Facilities supported by the National Science Foundation under Award No. DMR-9400379 and was partially supported by ONR-AASERT N00014-94-1-0798 and the National Science Foundation under Award No. DMS-9705912.

APPENDIX A: DERIVATION OF ASYMPTOTIC EQUATIONS

Here, we give a more complete derivation of the asymptotic equations. Substituting Eq. (2.18) into the scaled equations (2.12) yields the following equations at leading order;

$$\begin{aligned} -u_{0r} + v_{0\theta} + w_{0z} &= 0, \quad p_{0r} = 0, \\ -p_{0\theta} + v_{0rr} - \cos \theta &= 0, \quad -p_{0z} + w_{0rr} = 0. \end{aligned} \quad (A1)$$

The corresponding boundary conditions at leading order are

$$\left. \begin{array}{l} v_{0r}=0 \\ w_{0r}=0 \\ -p_0=B^{-1} \end{array} \right\} \text{ at } r=\eta, \quad \left. \begin{array}{l} v_0=1 \\ w_0=0 \\ u_0=0 \end{array} \right\} \text{ at } r=0. \quad (\text{A2})$$

Solving Eqs. (A1) and (A2) yields the leading order velocity and pressure variables,

$$\begin{aligned} u_0 &= -\frac{r^3}{6} \sin \theta + \frac{r^2}{2} (\eta \sin \theta - \eta_\theta \cos \theta), \\ v_0 &= r \left(\frac{r}{2} - \eta \right) \cos \theta + 1, \\ w_0 &= 0, \\ p_0 &= -B^{-1}. \end{aligned} \quad (\text{A3})$$

At order $O(\alpha)$, we get the following equations:

$$\begin{aligned} p_{1r} &= \sin \theta, \\ -p_{1\theta} + v_{1rr} &= \beta(-u_0 \partial_r + v_0 \partial_\theta + w_0 \partial_z) v_0 + r p_{0\theta} + v_{0r}, \\ -p_{1z} + w_{1rr} &= -\beta(-u_0 \partial_r + v_0 \partial_\theta + w_0 \partial_z) w_0 + w_{0r}, \\ -u_{1r} + v_{1\theta} + w_{1z} &= -(ru_0)_r + r w_{0z}, \end{aligned}$$

subject to the following boundary conditions:

$$\left. \begin{array}{l} v_{1r}=2\eta v_{0r}-v_0 \\ w_{1r}=\eta w_{0r} \\ -p_1=B^{-1}(\eta+\eta_{zz}+\eta_{\theta\theta}) \end{array} \right\} \text{ at } r=\eta, \quad \left. \begin{array}{l} u_1=0 \\ v_1=0 \\ w_1=0 \end{array} \right\} \text{ at } r=0.$$

These can be solved analytically for u_1 , v_1 , w_1 and p_1 ,

$$\begin{aligned} u_1 &= \int v_{1\theta} dr + \int w_{1z} dr - \frac{r^4}{6} \sin \theta \\ &\quad + \frac{r^3}{2} (\eta \sin \theta - \eta_\theta \cos \theta), \\ v_1 &= \left(\frac{1}{3} r^3 - r^2 \eta + \frac{3}{2} \eta^2 r \right) \cos \theta - \left(\frac{1}{2} r^2 - r \eta \right) \\ &\quad \times B^{-1} (\eta_\theta + \eta_{zz} \theta + \eta_{\theta\theta\theta}) - r + \beta v_{1l}, \\ w_1 &= \left(\frac{r^2}{2} - r \eta \right) \{ -\eta_z \sin \theta - B^{-1} (\eta_z + \eta_{zzz} + \eta_{\theta\theta z}) \}, \\ p_1 &= (r - \eta) \sin \theta - B^{-1} (\eta + \eta_{zz} + \eta_{\theta\theta}), \end{aligned}$$

where

$$\begin{aligned} v_{1l} &= \left(-\frac{1}{360} r^6 + \frac{1}{60} r^5 \eta - \frac{1}{24} r^4 \eta^2 + \frac{1}{10} r^5 \eta \right) \sin \theta \cos \theta \\ &\quad + \frac{1}{6} \left(\frac{1}{4} r^4 - \eta^3 r \right) (\eta \eta_\theta \cos^2 \theta - \sin \theta) - \frac{1}{2} \left(\frac{1}{3} r^3 - \eta^2 r \right) \\ &\quad \times (\eta \cos \theta)_\theta. \end{aligned}$$

v_1 and w_1 were used in Eq. (2.16) to obtain the final order α fluxes, Eqs. (2.19) and (2.20). Here we keep the terms of $O(B^{-1})$ even though capillarity is not important over most of the domain ($B^{-1} \ll 1$). However, in the vicinity of the front where the curvature is large, capillary forces are important.

APPENDIX B: NUMERICAL METHODS

We find it convenient to replace the fourth-order PDE by two second-order PDEs for η and $f = \eta_{\theta\theta}$. Both f and η are knot centered and the fluxes q and Q are calculated at the center of each interval using averaged variables so that

$$\eta_{i+\frac{1}{2},j} = \frac{1}{2} (\eta_{i,j} + \eta_{i+1,j}).$$

We use an implicit scheme for the time differencing where Δt is chosen by step doubling. The resulting equations are solved simultaneously via Newton's method using 1 or 2 iterations. We then use extrapolation to eliminate the first order error in Δt , i.e., if $C(\Delta t, k)$ is the solution at the end of k time steps of size $\Delta t/k$ of the backward difference scheme,

$$C_{\text{extrapolated}} = 2C(\Delta t, 2) - C(\Delta t, 1).$$

In the case of a stationary front, we use a stationary and nonuniform mesh whose resolution is increased in the neighborhood of the known location of the front. For nonsteady states, we use a stationary uniform mesh. As shown in Fig. 3, the nonstationary profiles are much more "smeared out" than the steady state profiles so added resolution in the neighborhood of the "front" is unnecessary.

In the case of three-dimensional flows, we solve Eqs. (2.15), (2.19), and (2.20) numerically in the parameter range corresponding to the axially unstable range. For the boundary conditions on both ends of the cylinder we use $Q=0$ (no flux out the ends), $v = \Omega r = \Omega R(1 - \alpha \tilde{r})$ (no-slip on the end caps in the θ direction), and $h_{zz}=0$. We choose a no-slip, no-flux condition on the ends of the cylinder. The model equations are not strictly valid in the neighborhood of the wall. However, within a few film thicknesses, the effects of this boundary layer are not important.

Here, as in the two-dimensional case, we used a finite difference method with a nonuniform mesh in θ and a uniform mesh in z . All three-dimensional calculations were carried out in the steady state parameter regime. We also found it necessary to upwind the θ flux at $z = \pm l$ (i.e., at the end caps) to stabilize the computation.

¹H. Benkreira, R. Patel, M. F. Edwards, and W. L. Wilkinson, "Classification and analysis of coating flows," *J. Non-Newtonian Fluid Mech.* **54**, 437 (1994).

²K. J. Ruschak and L. E. Scriven, "Rimming flow of a liquid in a rotating horizontal cylinder," *J. Fluid Mech.* **76**, 113 (1976).

³F. M. Orr and L. E. Scriven, "Rimming flow: Numerical simulation of steady, viscous, free-surface flow with surface tension," *J. Fluid Mech.* **84**, 145 (1978).

⁴K. J. Ruschak, "Coating flows," *Annu. Rev. Fluid Mech.* **17**, 65 (1985).

⁵R. E. Johnson, in *Engineering Science, Fluid Dynamics: A Symposium to Honor T. Y. Wu* (World Scientific, Singapore, 1990), pp. 435–449.

⁶S. T. Thoroddsen and L. Mahadevan, "Experimental studies of the instabilities in a partially filled horizontal rotating cylinder," *Exp. Fluids* **23**, 1 (1997).

⁷F. Melo, "Localized states in a film-dragging experiment," *Phys. Rev. E* **48**, 2704 (1993).

⁸T. B. Benjamin, W. G. Pritchard, and S. J. Tavener, "Steady and unsteady flows of a highly viscous liquid inside a rotating horizontal cylinder" (preprint, 1993).

⁹D. Vallette, G. Jacobs, and J. Gollub, "Oscillations and spatiotemporal chaos of one-dimensional fluid fronts," *Phys. Rev. E* **55**, 4274 (1997).

¹⁰H. E. Huppert, "Flow and instability of a viscous current down a slope," *Nature (London)* **300**, 427 (1982).

¹¹S. M. Troian, E. Herbolzheimer, S. A. Safran, and J. F. Joanny, "Finger-

- ing instabilities of driven spreading films," *Europhys. Lett.* **10**, 25 (1989).
- ¹²M. Rabaud, Y. Couder, and S. Michalland, "Wavelength selection and transients in the one-dimensional array of cells of the printer instability," *Eur. J. Mech. B/Fluids* **10**, 253 (1991).
- ¹³H. K. Moffatt, "Behavior of a viscous film on the outer surface of a rotating cylinder," *J. Mec.* **16**, 651 (1977).
- ¹⁴R. E. Johnson, "Steady-state coating flows inside a rotating horizontal cylinder," *J. Franklin Inst.* **190**, 321 (1988).
- ¹⁵H. Ockendon and J. Ockendon, *Viscous Flow* (Cambridge University Press, Cambridge, 1995).
- ¹⁶L. D. Landau and E. M. Lifshitz, *Fluid Mechanics*, 2nd ed. (Pergamon, New York, 1987).
- ¹⁷J. Guckenheimer and P. Holmes, *Nonlinear Oscillations, Dynamical Systems and Bifurcations of Vector Fields* (Springer, New York, 1983).
- ¹⁸Lord Rayleigh, *The Theory of Sound*, 2nd ed. (Dover, New York, 1945).
- ¹⁹T. E. Faber, *Fluid Dynamics for Physicists* (Cambridge University Press, Cambridge, 1997).
- ²⁰M. A. Spaid and G. M. Homsy, "Stability of Newtonian and viscoelastic dynamic contact lines," *Phys. Fluids* **8**, 460 (1996).
- ²¹J.-T. Jeong and H. K. Moffatt, "Free-surface cusps associated with flow at low Reynolds number," *J. Fluid Mech.* **241**, 1 (1992).
- ²²C. Ellegard, A. Hanse, T. Bohr, and S. Watanabe, "Corners in kitchen sink flows," *Nature (London)* **392**, 797 (1998).
- ²³H. Schlichting, *Boundary Layer Theory* (Pergamon, New York, 1955).